Interactions between infernan and calcium: From the molecular level to the mechanical properties of microgels

Agata Zykwinska, Olga Makshakova, Perrine Gélébart, Corinne Sinquin, Nicolas Stephant, Sylvia Colliec-Jouault, Serge Perez, Stéphane Cuenot

Interactions between infernan and calcium: from the molecular level to the mechanical properties of microgels

Agata Zykwinska,[a*] Olga Makshakova,[b] Perrine Gélébart,[a] Corinne Sinquin,[a] Nicolas Stephant,[c] Sylvia Colliec-Jouault,[a] Serge Perez[d] & Stéphane Cuenot[c*]

[a] Ifremer, MASAE, 44300 Nantes, France

[b] Kazan Institute of Biochemistry and Biophysics, FRC Kazan Scientific Center of RAS, Lobachevsky Str., 2/31, 420111 Kazan, Russian Federation

[c] Nantes Université, CNRS, Institut des Matériaux Jean Rouxel, IMN, Nantes, France

[d] Centre de Recherches sur les Macromolécules Végétales, Université de Grenoble Alpes, Centre National de la Recherche Scientifique, Grenoble, France

* Corresponding authors: Agata.Zykwinska@ifremer.fr, Tel.: +33-240-37-40-65; Stephane.Cuenot@cnrs-imn.fr, Tel.: +33-240-37-64-21.

Abstract

With the increasing need for hydrogels with tunable properties for specific biomedical applications, a complete understanding of the structure-function relationship of polymers used for hydrogel development remains crucial for their optimal use. In the present study, by combining experimental and theoretical approaches, the structure-function relationship of a bacterial exopolysaccharide, infernan, displaying both glycosaminoglycan-mimetic and gelling properties, was investigated at molecular and microscopic levels. Atomic force microscopy (AFM) experiments and molecular dynamics simulations were applied to determine the persistence length of individual infernan chains before studying their association induced by calcium. Infernan-based microgels were then produced using microfluidics and their

mechanical properties were characterized by AFM methods. The mechanical properties of EPS/calcium microgels were finely tuned by varying the crosslinking density of their network, either by calcium or EPS concentrations. The obtained set of viscoelastic microgels with different elastic modulus values opens several possibilities for their applications in tissue engineering.

Keywords

Atomic force microscopy, molecular dynamics simulations, persistence length, viscoelastic properties, microfluidics.

1. Introduction

Polysaccharides constitute a highly diverse family of macromolecules in primary and secondary structures, which further determine their valuable functional properties. Polysaccharides occur in plant (e.g. pectin, cellulose) and algal (e.g. alginate, carrageenan, fucan) cell walls, and in animal tissues (glycosaminoglycans, GAG). They are also secreted by microorganisms, including bacteria (e.g. xanthan, gellan, welan, hyaluronic acid). These ubiquitous macromolecules are essential for cells, tissues and the whole organism, in which they fulfil crucial structural and biological functions. Both structure and molecular weight of polysaccharides determine their functionalities, which are largely exploited in several domains. For instance, physicochemical, in particularly gelling, properties of some anionic heteropolysaccharides, such as alginate, pectin, carrageenan and xanthan, have been explored for many decades in food, cosmetics and more recently in biomedical applications (Augst, Kong, & Mooney, 2006; Freitas, Coimbra, Souza, & Sousa, 2021; Kumar, Rao, & Han, 2018; Pacheco-Quito, Ruiz-Caro, & Veiga, 2020). They contribute largely to the economy of glycoscience (Corolleur, Level, Matt, & Perez, 2020). The common feature of these polysaccharides is their ability to form a physical gel in the presence of divalent cations, e.g. calcium (Ca^{2+}). In the case of alginate, gel formation results from the association of single helical chains rich in guluronic acid (GulpA) domains into junction zones through the Ca^{2+} ions coordinated between them, as described in the "egg-box model" (Grant, Morris, Rees, Smith, & Thom, 1973). For pectin gelation, a modified model called the "shifted egg-box model" was proposed to explain the association of pectin domains rich in galacturonic acid (GalpA) into junction zones through Ca^{2+} (Braccini, & Pérez, 2001). In contrast to alginate and pectin, where carboxylic oxygen atoms and water oxygen coordinate the divalent ion, iota-carrageenan gelation results from inter-helix bridges stabilized by Ca^{2+} coordinated by negatively charged sulfate groups and water molecules (Janaswamy, & Chandrasekaran, 2008). Xanthan is an

example of a bacterial exopolysaccharide (EPS), having, in its repeating unit, a negatively charged trisaccharide side chain attached to a cellulose-like backbone (Jansson, Kenne, & Lindberg, 1975). In the helical conformation adopted by xanthan chains, the side chains remain aligned with the backbone and stabilize the overall structure by non-covalent interactions, mainly hydrogen bonding (Moorhouse, Walkinshaw, & Arnott, 1977). The presence of Ca^{2+} stabilizes xanthan in its ordered helical conformation, where the main binding sites are likely constituted between the terminal pyruvate groups of the side chains, while the main chains play a minor role in the cation complexation (Bergmann, Furth, & Mayer, 2008; Lambert, Milas, & Rinaudo, 1985). Recently, we have shown that a bacterial EPS secreted by the deep-sea hydrothermal vent bacterium *Alteromonas infernus*, called infernan (GY785 EPS), was also able to gel in the presence of Ca^{2+} (Zykwinska *et al*., 2019; Gélébart *et al*., 2022). Similarly to xanthan, infernan is also a highly branched heteropolysaccharide. However, its repeating unit is slightly more complex (Roger, Kervarec, Ratiskol, Colliec-Jouault, & Chevolot, 2004). The trisaccharide main chain, composed of glucose (Glcp), GalpA and galactose (Galp), is covalently linked in the sequence: →4)-β-D-Glcp-(1→4)-α-D-GalpA-(1→4)-α-D-Galp-(1→, is branched by a hexasaccharide side chain. Indeed, GalpA residue of the main chain is substituted at O-3 by two glucuronic acids (GlcpA), one Gal and one Glc giving the following sequence: β-D-Glcp-(1→6)-α-D-Galp-(1→4)-β-D-GlcpA-(1→4)-β-D-GlcpA-(1→. In addition, the two GlcpA of the side chain are each substituted by a terminal Glcp. The interesting feature of this EPS is its anionic nature resulting from the presence of uronic acid residues and sulfate groups. Indeed, GalA of the main chain is substituted at O-2 by one sulfate group. In contrast to xanthan, native infernan of high molecular weight (HMW), 2,000,000 g/mol, cannot gel. However, a physical Ca^{2+} gel was formed by a medium molecular weight (MMW) derivative, EPS DR (240,000 g/mol), obtained by radical depolymerization of the native HMW EPS (Zykwinska *et al*., 2019; Gélébart *et al*., 2022). Besides gelling properties with divalent cations, the negatively

charged EPS is also able to bind to positively charged proteins, such as basic growth factors, and this property has a huge potential in tissue engineering (Merceron *et al*., 2012; Rederstorff *et al*., 2017; Zykwinska *et al*., 2018; Zykwinska *et al*., 2019; Gélébart *et al*., 2022). Indeed, growth factors constitute a key element in tissue engineering strategies since they stimulate essential cellular processes (proliferation, migration, differentiation). Growth factor delivery systems, such as microgels, have intensely been explored to enhance growth factor bioactivity and sustain their local release to the surrounding microenvironment (Caballero Aguilar, Silva, & Moulton, 2019; Subbiah & Guldberg, 2019). By associating both physicochemical (gelling) and biological (GAG-mimetic) properties of infernan derivatives, we have recently developed growth factor-loaded microgels for cartilage and bone engineering purposes (Zykwinska *et al*., 2019; Gélébart *et al*., 2022).

The objective of the present study was to gain further insight into infernan (GY785 EPS) gelling properties induced by the presence of Ca^{2+}. The knowledge of the structure-function relationship remains crucial for the future development of infernan-based microgels for particular applications, especially in tissue engineering. For this purpose, polysaccharide-Ca^{2+} interactions were firstly studied at the molecular level by combining an experimental approach based on atomic force microscopy (AFM) with a theoretical one, exploiting molecular dynamics simulations. AFM constitutes a powerful tool allowing to image biological structures with nanometric resolution, to measure the forces between single molecules with piconewton sensitivity and to probe the mechanical properties (Cuenot, Bouvrée, & Bouchara, 2017; Florin, Moy, & Gaub, 1994; Hinterdorfer & Dufrêne, 2006; Zykwinska *et al*., 2018). Molecular dynamics simulations allowed to establish the molecular conformations of the polysaccharide chains upon Ca^{2+} binding. The impact of both EPS and Ca^{2+} concentrations on the mechanical properties of infernan-based microgels, formulated using capillary microfluidics, was further assessed by AFM measurements. The main hypothesis of the present study was how the

structure-function properties on the molecular level influence the mechanical properties of infernan-based microgels at the microscale.

2. Materials and Methods

2.1. Production of native infernan and medium molecular weight (MMW) EPS derivative (EPS DR_{MMW}), and their characterization

Native EPS was produced through fermentation (Raguénès *et al*., 1997). Briefly, *Alteromonas infernus* was cultured at 25°C pH 7.4 in a 30 L fermenter (Techfors 30 L INFORS, Switzerland) containing 20 L of Zobell medium, composed of 5 g/L of tryptone, 1g/L of yeast extract and 33.3 g/L of aquarium salts. For EPS biosynthesis, 30 g/L of glucose was added at the beginning of the batch. Native EPS excreted in its soluble form and remaining in the culture medium was recovered after 48h by a centrifugation step (9000 g, 45 min). The supernatant was then ultrafiltrated on a 100 kDa cut-off membrane and freeze-dried.

An EPS DR_{MMW} of 260,000 g/mol was prepared from native EPS using a free-radical depolymerization process (Gélébart *et al*., 2022). Native EPS and EPS DR_{MMW} were characterized for their monosaccharide composition, weight-average molecular weight and sulfur content (Gélébart *et al*., 2022).

2.2. Microgel formation by capillary microfluidics

EPS DR_{MMW} was structured into microgels using a home-made capillary microfluidic co-flow device (Figure S1). The dispersed phase containing EPS DR_{MMW} aqueous solution at 2, 3 or 4% (w/w) was delivered through a silica tube with an interior diameter of 75 µm inserted into chromatography tee fitting. The continuous phase, a sunflower seed oil (Fluka), was delivered through a Fluorinated Ethylene Propylene (FEP) 1/16" tube (ID 750 µm, OD 1.57 mm) (Cluzeau Info Labo, France) perpendicularly to the tee fitting. The dispersed phase co-flowed in a FEP 1/16" tube (ID 750 µm, OD 1.57 mm) containing the continuous oil phase.

The dispersed phase was applied at 2 µL/min and the continuous phase at 120 µL/min, to produce microdroplets. The flow rates were controlled using a Microfluidic Flow Control System MFCS^{TM}-EZ with a flow-rate platform (Fluigent). The device was run for 45 min per sample. Microdroplets were recovered in a collecting bath containing 10 mL of 360 mM (for EPS DR_{MMW} at 2, 3 and 4% (w/w)) or 1 000 mM $CaCl_2$ (for EPS DR_{MMW} at 4% (w/w)) under magnetic stirring to avoid their coalescence. Microgels formed directly upon the microdroplet contact with $CaCl_2$ solution were stored overnight at 4°C in either 360 mM or 1 000 mM $CaCl_2$. Microgel suspensions were washed three times with the same $CaCl_2$ solutions before AFM experiments. Microgels remaining in 360 mM $CaCl_2$ were also equilibrated in 2 mM $CaCl_2$ for 24h at 4°C.

2.3. Microscopy

Microgels recovered in collecting baths were observed using an optical microscope (Optika, Italy). The size of microgels (N = 30) was determined using Optika Vision Lite software. Scanning electron microscopy SEM observations on freeze-dried microgels were performed using JEOL JSM 7600F instrument (JEOL, Japan) working at an accelerating voltage of 5KV. Images were collected by the Everhart-Thornley secondary electron detector of the chamber, far enough of the lens to ensure good depth of field.

2.4. AFM

2.4.1. AFM imaging

For AFM imaging, EPS DR_{MMW} aqueous solution at 1 mg/mL was diluted at 5 µg/mL in water. For EPS DR_{MMW}/$CaCl_2$ samples, $CaCl_2$ aqueous solution at 10 mg/mL was mixed (1:1, v/v) with EPS DR_{MMW} aqueous solution at 1 mg/mL. The remaining mixture was then diluted in water at either 5 µg/mL or 50 µg/mL. Five µL of each diluted solution were deposited on freshly cleaved mica surface and left overnight to allow slow evaporation of water under

158 ambient conditions. These conditions favor a slow transition from the hydrated state to the dried
159 state, contrary to a quick-drying with pressurized air.

160 The surface of samples was systematically imaged on four zones using a NanoWizard®
161 Atomic Force Microscope (JPK, Germany) operating in air in intermittent contact mode. A
162 standard rectangular cantilever (Nanosensors NCL-W) with a free resonance frequency of 165
163 kHz and a spring constant of ~40 N/m was used. Before AFM observations, an AFM tip with a
164 radius curvature of ~10 nm was cleaned by UV-ozone treatment. High-resolution images (2 µm
165 x 2 µm, 2048 x 2048 pixels) were acquired for EPS DR_{MMW} samples, while lower resolution
166 (10 µm x 10 µm, 512 x 512 pixels) was applied for EPS $DR_{MMW}/CaCl_2$ samples. All images
167 were only flattened to remove the background curvature. The height measurements of
168 polysaccharide chains were performed using JPK Data Processing software (JPK, Germany).
169 A home-made Matlab program performed both histograms of measured heights and the
170 statistical analysis of adsorbed chains. After digitizing the EPS DR_{MMW} chain contours from
171 high-resolution AFM images, the mean square end-to-end distance $\langle R^2 \rangle$ was calculated by
172 varying the internal contour length (s) from the pixel size to the total length. Only nonlinear
173 single chains without overlapping or coiling were selected for these statistical measurements.
174 In addition, their contour lengths have to be higher than 145 nm (as the infernan chain length
175 was estimated at ~250 nm from the mean value of molecular weight) to avoid an overestimation
176 of the persistence length with shorter chains. The persistence length, L_p, was then determined
177 by fitting the experimental data ($\langle R^2 \rangle$ - s curve) by the 2D worm-like chain model using the
178 least-squares method (Bettini, Pozzan, Valdevit, & Frontali, 1980; Rivetti, Guthold, &
179 Bustamante, 1996). Only L_p values corresponding to the best fits (with a coefficient of
180 determination > 0.95) were used to calculate the mean value.

181

182

183 *2.4.2. Mechanical measurements on microgels*

184 Before mechanical measurements by AFM, microgels were immobilized on a Petri dish
185 glass surface functionalized with poly-L-lysine (PLL, Sigma). The glass surface was firstly
186 washed with ethanol before being exposed to UV-ozone treatment for 10 minutes. Then 200 µL
187 of PLL at 0.01% was deposited for 30 minutes. After washing with MilliQ water, the surface
188 was dried, and 20 µL of microgel suspension were deposited and incubated for 30 minutes. All
189 AFM experiments were performed in $CaCl_2$ at room temperature at different concentrations
190 (2mM, 360 mM and 1 000 mM). Indentation and relaxation experiments were carried out with
191 cantilevers (SQube) having a colloidal glass sphere of 5 µm in diameter. The cantilever spring
192 constant, calibrated using the thermal noise method implemented in the AFM setting (JPK
193 software), was comprised between 0.14 and 0.17 $N.m^{-1}$. Before indentation experiments,
194 several approach-retract force curves were performed on different microgels (for the chosen
195 $CaCl_2$ concentration) to accurately determine the force to be applied corresponding to an
196 indentation depth of ~500 nm. This depth corresponds to a good compromise to avoid the long-
197 range interactions and to be within the validity domain of the Hertz contact model. Then,
198 conventional force curves were recorded at a constant speed (1 µm/s) on microgels with a
199 maximum indentation depth of ~500 nm. This low cantilever velocity was chosen to neglect
200 the hydrodynamic drag forces (proportional to the cantilever velocity) exerted on the cantilever
201 when experiments are carried out in a liquid medium. These forces were then converted into
202 force-indentation curves, and the approach part was fitted by the Hertz model to determine the
203 apparent elastic modulus of microgels. Modified force curves were performed for micro-
204 rheological measurements by adding a holding phase of 3 s between the approach and retraction
205 parts (recorded at high speed, 20 µm/s). During the holding phase, the force relaxation was
206 measured over time while the indentation depth was kept constant at 500 nm within microgels.

The time-dependent shear relaxation modulus was then directly determined with the experimental parameters using the Lee-Radok equation (Lee & Radok, 1960).

2.5. Molecular dynamics simulations

The molecular dynamics simulations were performed using program package AMBER12 (Case *et al*., 2012) in the isotherm isobar thermodynamic ensemble at 300K, using the force-field parameters for GLYCAM06 for saccharides (Kirschner *et al*., 2008). The AMBER force field was used for ions and the TIP3 model for water molecules, following the protocol described previously (Makshakova, Zykwinska, Cuenot, Colliec-Jouault, & Perez, 2022) with trajectories in the range of 100 ns and output frequency of 10 ps. From the succession of glycosidic torsion angles extracted from the trajectory, chain samples having up to 1 000 monosaccharide units were constructed and processed.

3. Results and Discussion

3.1. Infernan-calcium interactions study at the molecular level by AFM imaging and molecular dynamics simulations

Native EPS characterized by its very high molecular weight (2,000,000 g/mol) could not gel in the presence of Ca^{2+} (Zykwinska *et al*., 2019). Long thick fibres previously observed by AFM prevented most likely from efficient chain-chain associations and formation of stable junction zones necessary for gelling. In contrast, EPS derivative of medium molecular weight (EPS DR_{MMW}), 240,000 g/mol, prepared by free-radical depolymerization of the native EPS, formed a gel with Ca^{2+}. An increase in fibre diameter was observed after Ca^{2+} addition, emphasizing that the formation of stable junction zones was favored by shorter polysaccharide chains (Zykwinska *et al*., 2019). In the present study, to gain further insight into the ability of infernan derivatives to form a physical gel, EPS/Ca^{2+} interactions were firstly investigated at the molecular level using dual, experimental (AFM) and simulation (molecular dynamics)

approach. For the experimental part, EPS DR_{MMW} of 260,000 g/mol was prepared by free-radical depolymerization of native EPS. The depolymerization reaction had no significant impact on the polysaccharide composition (Gélébart *et al*., 2022). From the consideration of the infernan derivative molecular weight and the molar mass of the nonasaccharide repeating unit (1 567 g/mol), it can be estimated that infernan chains contain around 166 repeating units of ~250 nm in length.

3.1.1. Persistence length of infernan derivative

AFM and molecular dynamics simulations were first applied to investigate the conformational behavior of individual EPS chains before calcium addition. High-resolution AFM imaging in the air was largely used to visualize the conformations of various flexible (bio)polymers and filaments such as DNA, amyloid fibrils and polysaccharide chains (Morris *et al*., 2001; Rivetti *et al*., 1996; Relini *et al*., 2010; Schefer, Usov, & Mezzenga, 2015; Zykwinska *et al*., 2018; Zykwinska *et al*., 2019). The usually applied method consists in deposition of diluted solution on a flat substrate to favor isolated chains before imaging in a dry state. Figure 1A presents dried, highly-diluted EPS DR_{MMW} solution (5 µg/mL), showing the worm-like behavior of EPS chains in 2D. The distribution of measured heights revealed that mainly individual monomolecular chains of 0.54 ± 0.07 nm in height were observed (Figure 1B). Similar results have been reported for other anionic polysaccharides, such as alginate, pectin, xanthan or gellan (Decho, 1999; Morris *et al*., 2001; Schefer *et al*., 2015; Zdunek, Pieczywek, & Cybulska, 2021; Zykwinska, Gaillard, Boiffard, Thibault, & Bonnin, 2009).

Before characterizing the 2D conformations adopted by infernan chains, it seems essential to determine how the adsorption affects the chain conformation. During the deposition process, the conformational changes induced by the transition from free three-dimensional (3D) chains remaining in solution to chains adsorbed on the surface depend on the polysaccharide-substrate interaction strength. Indeed, in the case of weak interactions, chains can freely relax and are

fully equilibrated on the surface. The resulting 2D equilibrated conformations can be treated with the same formalism of free chains in solution (Rivetti *et al*., 1996). Conversely, chains are kinetically trapped on the surface without equilibrating when strong interactions occur and the adopted 2D conformations reflect the history of chain-surface contact points. These non-equilibrated chain conformations are expected to correspond to the projection of 3D chain conformations to the surface (Bettini *et al*., 1980; Rivetti *et al*., 1996). In our case, weak interactions between infernan chains and hydrophilic mica surface involving hydrogen bonds and van der Waals interactions will favor 2D equilibrated chain conformations on the substrate. Such an equilibrated behavior was observed for another anionic polysaccharide, carrageenan, adsorbed on a positively charged mica surface. This mica functionalization led to an increase of electrostatic interaction contribution, which favored chain immobilization on the surface without preventing carrageenan chains from adopting 2D equilibrated conformations (Schefer *et al*., 2015).

A statistical analysis of geometrical shapes of individual infernan chains was then performed by measuring the 2D mean-square end-to-end distance ($\langle R^2 \rangle$) from AFM images. In Figure 1C, the plot of $\langle R^2 \rangle$ as a function of the internal contour length, *s*, (*i.e*. the distance between two contour segments describing the chain) is reported for *s* varying between the pixel size (~0.97 nm) and the total contour length. This $\langle R^2 \rangle$ - *s* relationship can be theoretically expressed for semi-flexible polymer chains by the 2D worm-like chain (WLC) model with the following equation (Bettini *et al*., 1980; Rivetti *et al*., 1996):

$$\langle R^2 \rangle = 4L_P\left(s - 2L_P\left(1 - \exp^{-\frac{s}{2L_P}}\right)\right) \quad (1)$$

where L_p is the polymer persistence length. This physical parameter is defined as the characteristic length scale over which the tangent vectors along the chain contour correlate, usually attributed to the local resistance of the chain to bending (Bettini *et al*., 1980). The

persistence length was then determined as the only adjustable parameter by fitting the $<R^2>$ experimental data by equation (1) using the least-squares method. The excellent agreement between experimental and theoretical $<R^2>$ - *s* dependence indicates a good description of 2D infernan chains by the 2D WLC model (Figure 1C). An average L_p value of 24.8 ± 7.6 nm was determined from these fits performed on 22 single infernan chains with contour lengths ranging from 145 nm to 275 nm, in accordance to the chain length of ~250 nm estimated from infernan molecular weight. The obtained L_p value is in good agreement with published values using the same AFM method, such as L_p values for carrageenan chains without calcium comprised between 17 nm (lambda carrageenan) and 32 nm (iota and kappa carrageenans) (Schefer *et al.*, 2015). Alkali-soluble pear pectin displayed the persistence length of 129 ± 92 nm in water, assessed by AFM (Cieśla *et al.*, 2021).

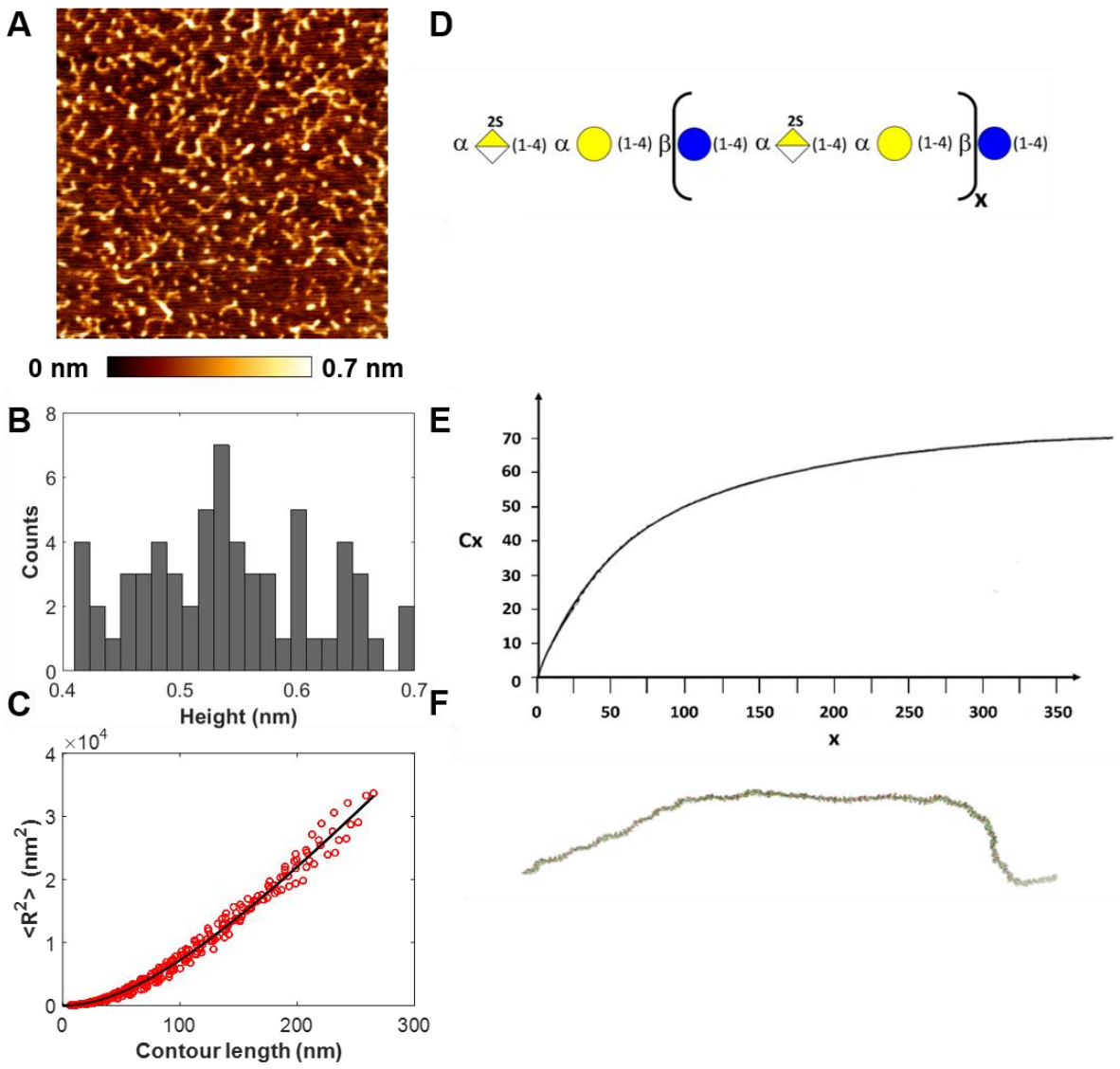

Figure 1. (A) AFM height image (2 µm x 2 µm) of EPS DR_{MMW} single chains. EPS DR_{MMW} at 5 µg/mL in water deposited on a mica surface and imaged in intermittent contact mode in air after drying. (B) Height distribution of imaged EPS DR_{MMW} chains and (C) mean-square end-to-end distance ($<R^2>$) measured on a single chain from AFM image as a function of the contour length. The dark line corresponds to the theoretical relation of the 2D worm-like chain model. (D) Schematic representation of the backbone structure of infernan, where the monosaccharides are depicted following the SNFG representation. (E) Variation of the characteristic ratio, C_x as a function of x, being the number of infernan repeating units. (F) Snapshot of a typical infernan chain containing 300 repeating units.

The persistence length, L_p of a polysaccharide can be calculated from molecular modelling results. Figure 1D shows a schematic representation of the backbone structure of infernan using

the SNFG representation for the monosaccharides by specifying the repeating unit, *x*. Because of the spatial separation afforded by the rigid sugar residues which are interpolated between the flexible linkages, the independence of the sets of glycosidic torsional angles from neighboring sets within the polysaccharide chain is a valid assumption, at least as a first approximation, for almost all glycosidic linkage types except a (1→2) linked monosaccharides. Therefore, the configurational energy for the macromolecular chains is decomposed into additive contributions from the conformational energy of adequately chosen segments such as dimeric fragments. Spatial representative polysaccharide chains are described by specifying values for all torsion angles (Φ, Ψ) of the set (Brant & Goebel, 1975). Assuming that interactions between monosaccharides further away than the first neighbors are not significant, a chain sample may be generated by confining examination to the conformations occurring at the glycosidic linkages. One way to perform such a task is to extract the values of the consecutive glycosidic linkages from the molecular dynamics simulation trajectories and assess these values to a continuously growing polysaccharide chain (Kroon-Batenburg, Kruiskamp, Vliegenthart, & Kroon, 1997). In the generation, no effort is made to eliminate long-range excluded-volume interactions. Each set of torsion angles is assumed to occur independently from all the rest. Therefore, a chain of *p* residues can be considered as consisting of (*p*-*x*) independent chains of a degree of polymerization, *x*, for which the properties may also be evaluated. The persistence length, L_p was calculated from the characteristic ratio C_∞, a dimensionless descriptor valid to compare unperturbed polymers chain dimensions (*i.e.* dimensions of a macromolecule subjected to only short-range interactions) of different polysaccharides, corresponding to the asymptotic behavior of C_x (*i.e.* obtained for high values of *x*). The smaller the C_∞ value, the more flexible a polymer chain. The characteristic ratio, C_x, defined in function of *x*, is evaluated using the following equation:

$$C_x = \frac{1}{Nxl_0^2}\sum_{k=1}^{N} r^2 k \qquad (2)$$

where N is the number of chains, k is the number of samples, and l_o is the average virtual bond length connecting glycosidic oxygens. The virtual bond lengths were derived from the conformation analysis. The characteristic features of the main backbone of infernan chain in its random conformation were simulated for chain samples having up to 1 000 monosaccharides. In Figure 1E, C_x first increases as a function of x and becomes independent of x when the asymptotic behavior is reached for about 300 repeating units. The corresponding infernan chain containing 300 repeating units is presented in Figure 1F. The specific value C_∞ determined from Figure 1E is about 65 indicating a significant extension of the infernan chain. This behavior closely resembles that calculated for homogalacturonan and some other (1→4)-linked uronic acid-rich polysaccharides (Braccini, Grasso, & Perez, 1999), since it arises from the similarity of the sequence of linkages between the main backbone of infernan and uronic acids. The persistence length, L_p can then be calculated from $L_p = l_0 C_\infty/2$ (Kroon-Batenburg *et al*., 1997). A value of 140 Å was found for the persistence length of the infernan chain. Similar simulated values were reported for homogalacturonan (140 Å, 110 Å), cellulose (145 Å) or more flexible hyaluronan (75 Å) (Cros, Garnier, Axelos, Imberty, & Perez, 1996; Noto, Martorana, Bulone, & San Biagio, 2005; Kroon-Batenburg *et al*., 1997; Haxaire, Braccini, Milas, Rinaudo, & Perez, 2000). The persistence length of infernan chains calculated from the molecular dynamics simulations on free chains in solution, with the L_p value of 14 nm, agreed with the value obtained from AFM imaging of 24.8 ± 7.6 nm. This confirmed the correct assumption that imaged chains were fully equilibrated on the substrate before AFM imaging.

352 *3.1.2. Chain-chain associations through calcium ions*

353 AFM imaging was firstly performed on highly-diluted EPS DR_{MMW}/Ca^{2+} solution (5
354 µg/mL) dried on a mica surface to investigate infernan chain-chain associations induced by
355 Ca^{2+} (Figure 2A). Histogram of measured heights from AFM images clearly revealed three
356 distinct peaks at 0.55 ± 0.07 nm, 1.04 ± 0.09 nm and 1.49 ± 0.07 nm. The imaged network of
357 highly branched fibers suggested that despite monomolecular chains of ~0.5 nm in height,
358 several chains associated with Ca^{2+} were also present. Less-diluted EPS DR_{MMW}/Ca^{2+} solution
359 (50 µg/mL) offered an opportunity to observe a dense network setting (Figure 2B). Height
360 measurement on these fibers indicated a further increase in their diameters from ~5 nm to ~10
361 nm, highlighting additional chain-chain associations. The branching points displayed the same
362 height as fibers in their linear parts.

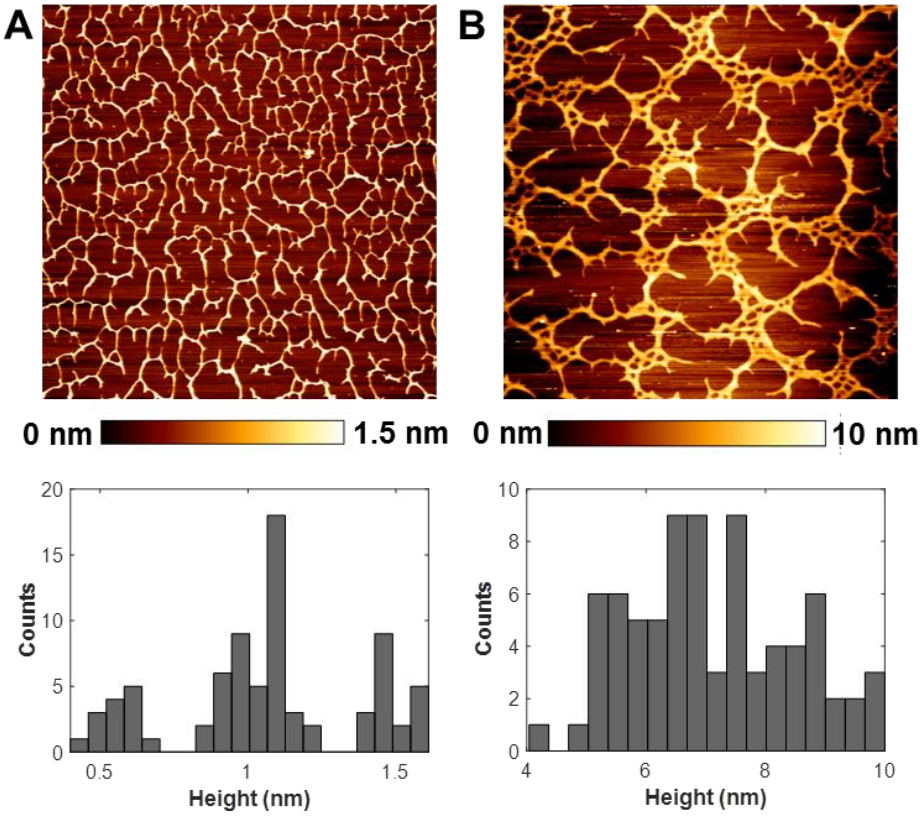

363 Figure 2. AFM height images (10 µm x 10 µm) and height distribution: (A) EPS $DR_{MMW}/CaCl_2$ solution
364 diluted at 5 µg/mL and (B) EPS $DR_{MMW}/CaCl_2$ diluted at 50 µg/mL. All sample solutions in water were
365 dried on a mica surface at 20°C before imaging in intermittent contact mode in air.

366 To better understand chain-chain association induced by Ca^{2+} leading to the formation of a
367 stable and homogeneous network observed by AFM, molecular dynamics simulations were
368 performed. We have recently reported that the disordered state of the infernan macromolecule
369 displays a continuous series of pseudo helical segments exhibiting either around a two-fold or
370 a five-fold structure (Makshakova *et al*., 2022). It was shown that the side chains of infernan
371 are essential for creating the Ca^{2+} chelating sites in the region of the branching point involving
372 three adjacent residues: βGlcp and αGalpA-2S from the backbone and βGlcpA from the side
373 chain. Our previous computations showed that only the two-fold helical shape and its
374 subsequent ribbon-like structure allows bringing neighboring chains in proximity without steric
375 conflicts. The two-fold helical conformation of the backbone, presenting the appropriate Ca^{2+}
376 cavity, may induce the formation of the polysaccharide chain pairing, providing the chains in
377 their favorable orientation. The coordination of Ca^{2+} within one chain reaches completion with
378 the oxygen atoms of a sulfate group belonging to the neighboring chain. The resulting "junction
379 zone" is based on chain-chain interactions that lead to strong dimer associations with essential
380 contributions from the van der Waals and hydrogen bonding interactions. Calcium ions, sulfate
381 groups and uronic acids have specific positions in well-adapted cavities (Makshakova *et al*.,
382 2022). The feature of the interaction is the heterotypic mode of binding, which contrasts with a
383 monotypic type of interactions characteristic of the binding mode of anionic polysaccharides,
384 such as alginate and pectins described by the "egg-box" model (Braccini & Perez, 2001). Such
385 a chain-chain association can propagate and result in the formation of rigid elements.
386 The models of chain-chain pairing induced by Ca^{2+} involving two adjacent polysaccharide
387 chains are presented in Figure 3A. Both lateral and twisted chain stacking conformations are
388 possible. Chain-chain associations can further continue, leading to several chains stacking
389 together (Figure 3B). The height of the two stacking chains is around 1.6 nm, while eight
390 stacking chains measure 6.5 nm in height. The obtained values are close to those measured from

AFM images of highly-diluted (5 µg/mL) and less-diluted (50 µg/mL) EPS DR_{MMW}/Ca^{2+} solutions (Figure 2). In highly-diluted solutions, the fiber height corresponds to a pairing of at least two chains, while in less-diluted solutions, the fiber height suggests stacking of more than six polysaccharide chains. Twisted helical conformations that may adopt two adjacent chains explain the formation of the complex network of connected fibers observed in Figure 2.

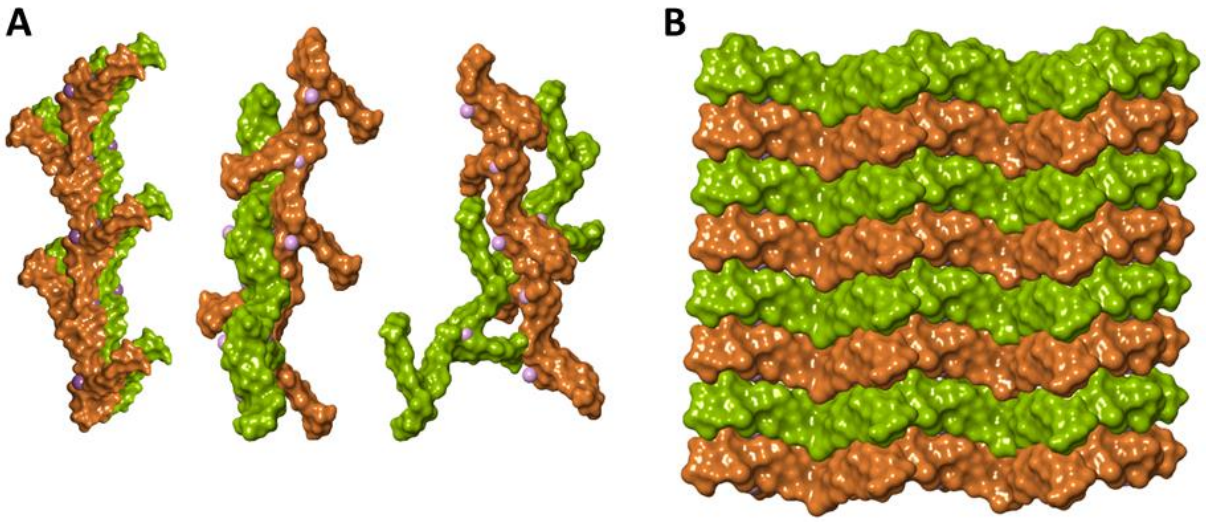

Figure 3. The models of infernan chain-chain stacking through Ca^{2+} ions. (A) Lateral and twisted pairings of two polysaccharide chains. (B) The lateral pairing of eight polysaccharide chains. The adjacent polysaccharide chains are displayed as surfaces in green and brown color; the Ca^{2+} ions are given as van der Waals spheres in violet.

3.2. Impact of infernan-calcium interactions on the mechanical properties of microgels

3.2.1. Microgel formation by capillary microfluidics

In the following step, the impact of infernan chain-chain associations mediated by Ca^{2+} on the mechanical properties of EPS-based microgels was studied. Such microgels were previously designed for growth factor encapsulation and release for tissue engineering applications (Zykwinska *et al*., 2019; Gélébart *et al*., 2022). Indeed, the mechanical properties of hydrogels deeply affect the release properties of encapsulated bioactive molecules and regulate essential cellular processes, including migration, proliferation and differentiation (Vinning, & Mooney, 2017). These properties are related to the hydrogel network nature determined by chemical

409 (covalent) or physical (non-covalent) crosslinks and their density. Herein, the impact of both
410 EPS and $CaCl_2$ concentrations on mechanical properties of physical microgels was investigated
411 using AFM. EPS DR_{MMW} aqueous solutions at three concentrations (2, 3 and 4% (w/w)) were
412 formulated into microdroplets using a homemade capillary microfluidic co-flow device (Figure
413 S1 and 4). Microdroplets formed inside a microfluidic device were recovered in the collecting
414 bath containing either 360 mM $CaCl_2$ (for EPS DR_{MMW} at 2, 3 and 4% (w/w)) or 1 000 mM
415 $CaCl_2$ (for EPS DR_{MMW} at 4% (w/w) only) under rapid magnetic stirring to avoid their
416 coalescence. Gelation of the EPS was initiated immediately after microdroplet contact with
417 $CaCl_2$ solution, which additionally decreased the coalescence phenomenon.

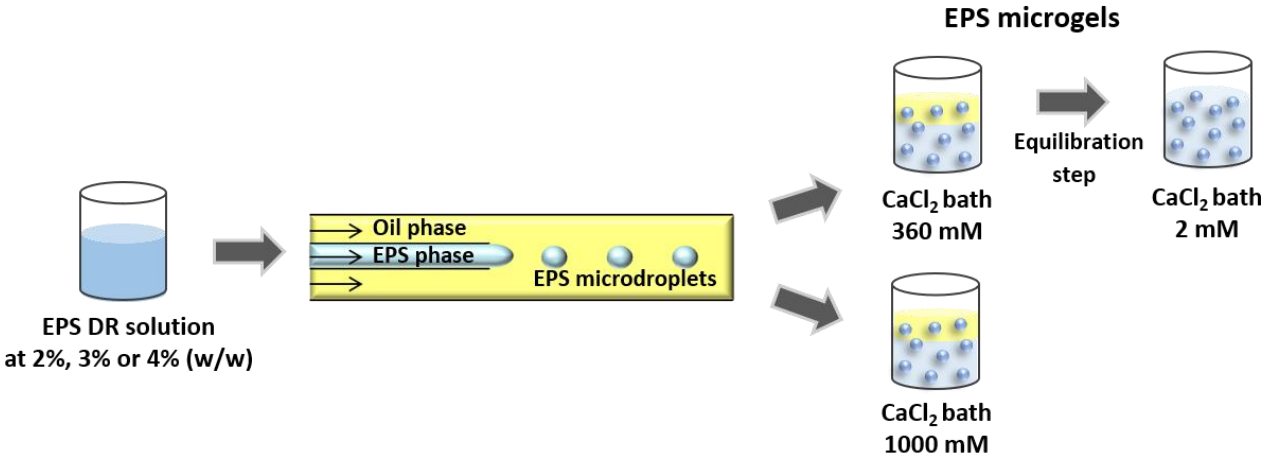

418 Figure. 4. Schematic representation of EPS DR_{MMW} based microgel formulation using capillary
419 microfluidics. EPS DR_{MMW} aqueous solution was used for microgel formulation at three different
420 concentrations: 2, 3 or 4% (w/w). The EPS microdroplets formed inside a microfluidic device gelled
421 immediately after their recovery in either 360 mM or 1 000 mM $CaCl_2$ collecting bath. In addition, an
422 equilibration step in 2 mM $CaCl_2$ was applied to microgels formed in 360 mM $CaCl_2$ to reach a
423 physiological calcium concentration.

424 Monodisperse microgels of 450 ± 61 µm, 463 ± 63 µm and 485 ± 54 µm in diameter were
425 obtained for EPS DR_{MMW} solutions at 2, 3 and 4% (w/w) in 360 mM $CaCl_2$, respectively (Figure
426 5A). Microgels crosslinked in 360 mM $CaCl_2$ were also equilibrated in 2 mM $CaCl_2$ for a further
427 24h to reach a physiological calcium concentration within the microgels (Figure 5B). During

this ionic concentration change, the density of cross-links between polysaccharide chains mediated by Ca^{2+} ions decreased, leading to a looser network compared to the initial network formed in 360 mM $CaCl_2$. This equilibration step led to a weak microgel swelling since an increase in microgel diameter was observed: 537 ± 89 µm, 535 ± 53 µm and 593 ± 77 µm for EPS DR_{MMW} solutions at 2, 3 and 4% (w/w), respectively (Figure 5B).

Microgels prepared from an EPS DR_{MMW} solution at 4% (w/w) and recovered in the calcium bath of the highest concentration (1 000 mM $CaCl_2$) were of 557 ± 58 µm in diameter. No significant differences in morphologies were noticed between microgels recovered in different calcium baths, as revealed by SEM (Figure 5C). In all cases, a porous structure was clearly observed with the presence of large fibers of ~100 to ~250 nm in width. These thick fibers result from further chain-chain associations mediated by Ca^{2+} ions taking place in microgels prepared at higher EPS and $CaCl_2$ concentrations, when compared to diluted samples prepared for AFM imaging.

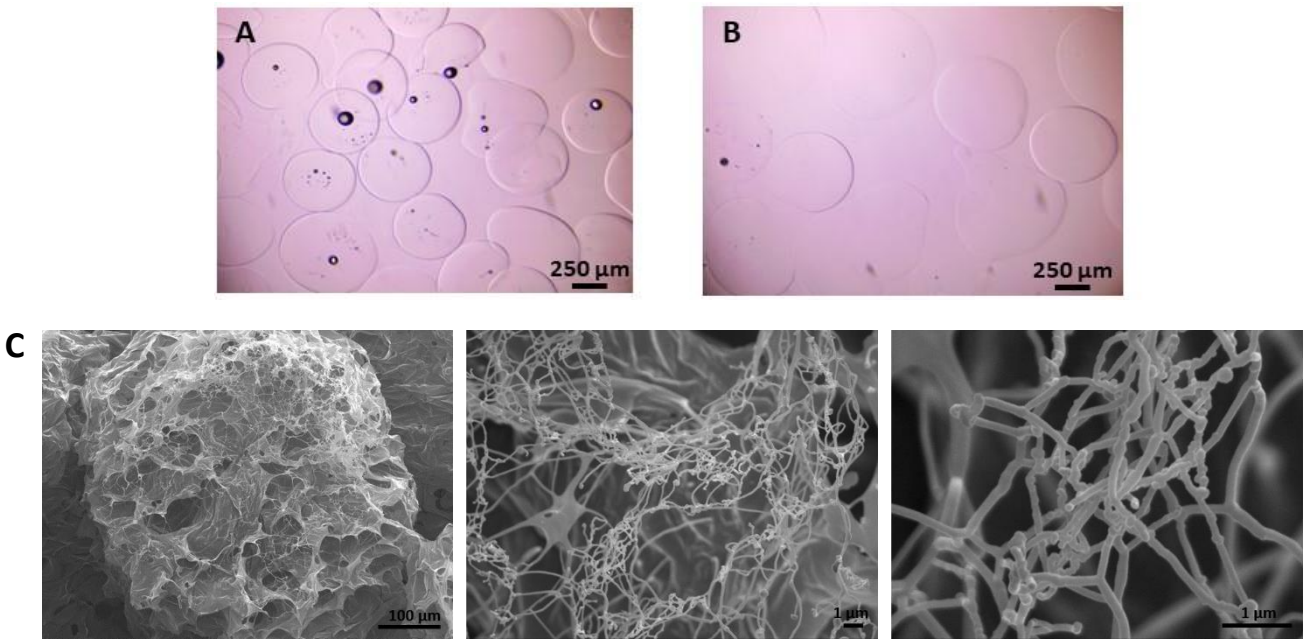

Figure 5. Optical images of EPS DR_{MMW} microgels at 4% (w/w) recovered in 360 mM $CaCl_2$ (A) and equilibrated in 2 mM $CaCl_2$ for 24h (B). Scanning Electron Microscopy (SEM) images of freeze-dried EPS DR_{MMW} microgels at 4% (w/w) recovered in 360 mM $CaCl_2$ (C).

3.2.2. Mechanical properties of microgels by AFM

Unlike macroscopic hydrogels for which rheological measurements give a direct access to their mechanical properties, determining these properties at microscale is more challenging. Over the last twenty years, the development of AFM-based methods has opened different ways to investigate the local mechanical properties of soft nano- and micrometer- sized samples (Berry, Biviano, & Dagastine, 2020; Cuenot, Alem, Louarn, Demoustier-Champagne, & Jonas, 2008; Cuenot, Radji, Alem, Demoustier-Champagne, & Jonas, 2012; Moreno-Guerra *et al*., 2019). Indeed, mechanical properties can be measured by operating either in the time or frequency domains through conventional force curves, force/indentation modulation, creep or force relaxation (Moreno-Guerra *et al*., 2019; Efremov, Okajima, & Raman, 2020). In the present work, combined AFM methods were used to characterize the mechanical properties of microgels. Firstly, microgels were indented by a glass sphere of 5 µm in diameter at ~500 nm to obtain conventional force (F)-indentation (δ) curves (Figure 6). Figure 6C shows the approach-retract F-δ curves obtained for three microgels formulated at 4% (w/w) and recorded in 2 mM, 360 mM or 1 000 mM $CaCl_2$. The Hertz model was then used to fit the approach curves to extract the apparent elastic modulus, E_{Hertz} (Hertz, 1881), which characterizes the ionic crosslinking density of microgels, *i.e.* the number of junction zones formed between infernan chains, involving sulfate and carboxylic groups, and calcium ions, as previously described (Makshakova *et al*., 2022). A good agreement between fitted and experimental curves was obtained for the different experimental conditions.

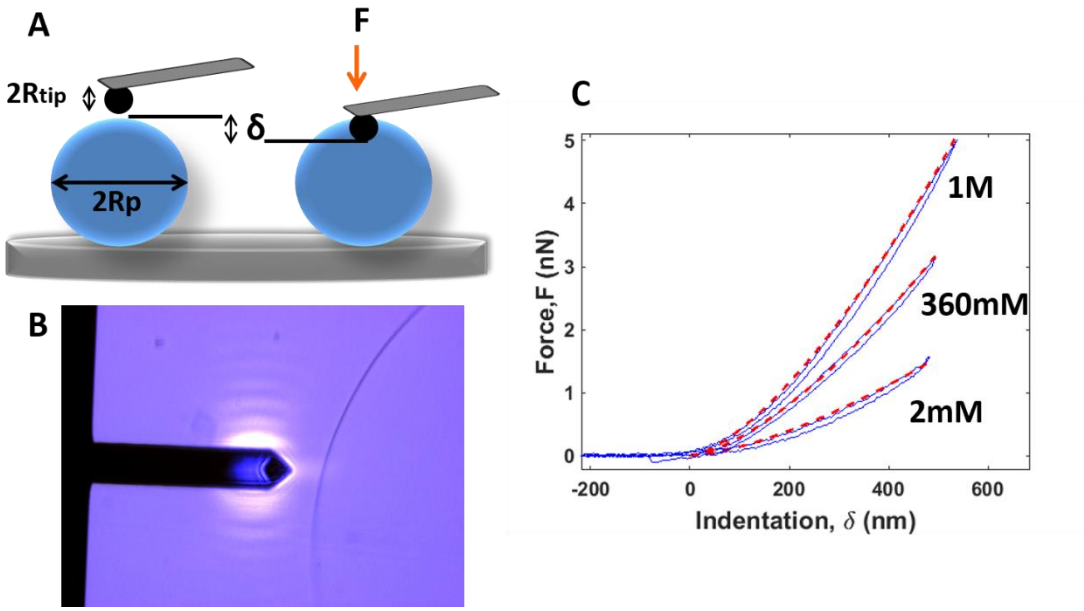

Figure 6. (A) Schematic representation of the experimental setup where a microgel of radius R_p is indented by a depth δ by a spherical probe of radius R_{tip} attached to an AFM cantilever. (B) Optical image showing the curvature of a probed microgel compared with the length of 225 µm (width 48 µm) of a used cantilever. (C) Experimental approach-retract force-indentation curves (in blue) were performed in different $CaCl_2$ solutions (2 mM, 360 mM and 1 000 mM) with Hertz's model fit (in red) of the approach curve.

The influence of the calcium concentration on the resulting apparent elastic modulus, E_{Hertz}, measured on 5 to 7 microgels at fixed EPS DR_{MMW} concentration (4% (w/w)) was presented in Figure 7A. E_{Hertz} increased with increasing calcium concentration from 1.4 ± 0.2 kPa at 2 mM to over 3.3 ± 0.1 kPa at 360 mM, and then to 7.6 ± 0.4 kPa at 1 000 mM $CaCl_2$, indicating that the crosslinking density increased with the ionic strength. A five-fold increase in the elastic modulus of microgels was observed between 2 mM and 1 000 mM $CaCl_2$. It appeared further that the equilibration step applied to the microgels to reach a physiological calcium concentration (from 360 mM to 2 mM $CaCl_2$) led to about a two-fold decrease in the elastic modulus. Such a decrease results most likely from the loss of calcium initially present within microgels, directly impacting the crosslink density of the network.

It was further observed that increasing EPS DR_{MMW} concentration at a fixed calcium concentration (360 mM $CaCl_2$) led to an increase in E_{Hertz} of microgels from 0.75 ± 0.15 kPa at 2% (w/w) to over 1.2 ± 0.1 kPa at 3% (w/w), and then to 3.3 ± 0.2 kPa at 4% (w/w) (Figure 7B). Therefore, the mechanical properties of microgels can also be tuned by the EPS concentration, as a two-fold increase in EPS concentration, from 2 to 4% (w/w), led to a four-fold increase in apparent elastic modulus.

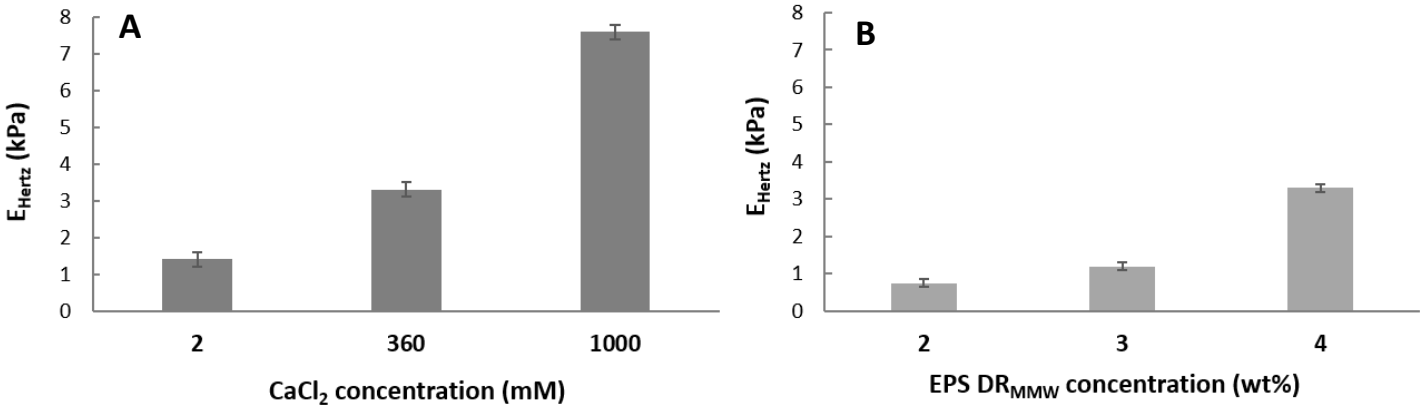

Figure 7. (A) The impact of $CaCl_2$ concentration (2, 360, 1 000 mM) on the apparent elastic modulus (E_{Hertz}) at constant EPS DR_{MMW} concentration (4% (w/w)). (B) The impact of EPS DR_{MMW} concentration (2, 3 and 4% (w/w)) on the apparent elastic modulus (E_{Hertz}) at constant $CaCl_2$ concentration (360 mM).

A hysteresis occurring between the approach and retraction F-δ curves observed in Figure 6C indicates that microgels exhibit time-dependent mechanical properties instead of purely elastic behaviour. Indeed, hydrogels possess both solid- and liquid-like features indicating that the mechanical energy is stored and dissipated, respectively. Thus, their behavior is somewhere between a purely elastic and strictly viscous material. For macroscopic hydrogels, the straightforward approach is to characterize these viscoelastic properties by determining the complex shear modulus, $G^*(w)$, by rheological oscillatory measurements over a broad range of discrete frequencies. AFM-based experiments have been conducted for micrometer-sized

hydrogels to determine their frequency-dependent viscoelastic properties using force/indentation modulation methods (Mahaffy, Park, Gerde, Kas & Shih, 2004; Xu, Koslowski & Raman, 2012; Nalam, Gosvami, Caporizzo, Composto & Carpick, 2015). An alternative to these frequency-dependent measurements is to perform modified force curves by adding a holding phase between the approach and retraction parts and recording the force relaxation over time while the indentation depth is kept constant (Darling, Zauscher, Block, & Guilak, 2007). In the present work, we investigated the frequency-dependent behavior of the elastic and viscous components for microgels with two extreme elastic modulus values, *i.e*. for the EPS DR_{MMW} concentration of 2 and 4% (w/w) (Figure 7B). The time-dependent shear relaxation modulus of the sample, $G(t)$, can be directly obtained from the force measured over time, $F(t)$, using the relation introduced by Lee and Radok for a spherical rigid indenter penetrating a viscoelastic sample (Lee & Radok, 1960):

$$F(t) = \frac{8\delta_0^{3/2}}{3(1-\nu)}\left[\left(\frac{1}{R_{tip}}\right)^{1/3} + \left(\frac{1}{R}\right)^{1/3}\right]^{-3/2} G(t) \qquad (3)$$

where δ_0 is the constant indentation depth, ν is the Poisson's ratio of the microgel, R_{tip} and R are the tip radius and the microgel radius, respectively. In our experiments, the following parameters were used: R_{tip} = 2.5 µm, R = 230 µm, δ_0 = 500 nm and ν = 0.5 as the widely accepted value for hydrogels (Moreno-Guerra *et al*., 2019, Efremov *et al*., 2020). Interestingly, $G(t)$ directly corresponds to the evolution of $F(t)$ as the constant of proportionality in equation (3) is fully determined by the experimental conditions (Moreno-Guerra *et al*., 2019). Figure 8A shows the raw data obtained for the shear relaxation modulus of microgels at 2 and 4% (w/w). An attractive approach to determine the viscoelastic properties of microgels, as an alternative of modulation methods, consists of performing the Fourier transform of the time derivative of $G(t)$ leading to $G^*(w)$, where w denotes the angular frequency (Evans, Tassieri, Auhl, & Waigh, 2009; Moreno-Guerra *et al*., 2019). Contrary to the direct analysis of force relaxation curves,

this transformation into the frequency regime avoids the use of viscoelastic constitutive models. The real, $G'(w)$, and imaginary, $G''(w)$, components of the complex shear modulus, describe the frequency-dependent elastic (storage modulus) and viscous (loss modulus) characters of the sample respectively. To calculate $G'(w)$ and $G''(w)$ from experimental data, the analytical procedure of Fourier transform, developed by Evans *et al*., was applied to equation (3) (Evans *et al*., 2009; Moreno-Guerra *et al*., 2019). This approach offers the advantage to control the range of accessible, continuous frequencies by the experimental temporal window. Indeed, the lowest frequency is related to the relaxation duration (*i.e*. 3 s), and the highest frequency is determined from the inverse of the sampling rate (*i.e*. the time-step). To increase this highest frequency, cubic spline interpolation of experimental $G(t)$ was performed before the Fourier transform to reduce the time-step from 0.01 s to 0.005 s (Figure 8A). Finally, the viscoelastic properties of microgels are available over several decades of continuous angular frequencies between 0.33 Hz and 200 Hz. No significant dependence on the frequency in the examined frequency range was observed for the storage modulus and the loss modulus obtained for microgels at 2 and 4% (w/w) (Figure 8B). $G'(w)$ and $G''(w)$ values were both higher for microgel at 4% (w/w) ($G'(w) \sim 1\,000$ Pa) compared to 2% (w/w) ($G'(w) \sim 250$ Pa), in agreement with the elastic modulus values measured from force-indentation curves (Figures 6 and 7). Indeed, a factor of about 3 exists between the storage modulus and the elastic modulus in the case of hydrogels ($G' = E/2(1+\nu)$ with $\nu \sim 0.5$), (Efremov *et al*., 2020). G' and E_{Hertz} were about 250 Pa and 750 Pa for microgels at 2% (w/w) while these values were respectively of 1 kPa and 3.3 kPa for microgels at 4% (w/w). In addition, no crossover occurred between these two moduli, with $G'(w)$ always higher than $G''(w)$, indicating that the solid-like behaviour of microgels was more pronounced than the liquid-like character. The small hysteresis appearing in the force-indentation curves (Figure 6C) tends also to confirm this result.

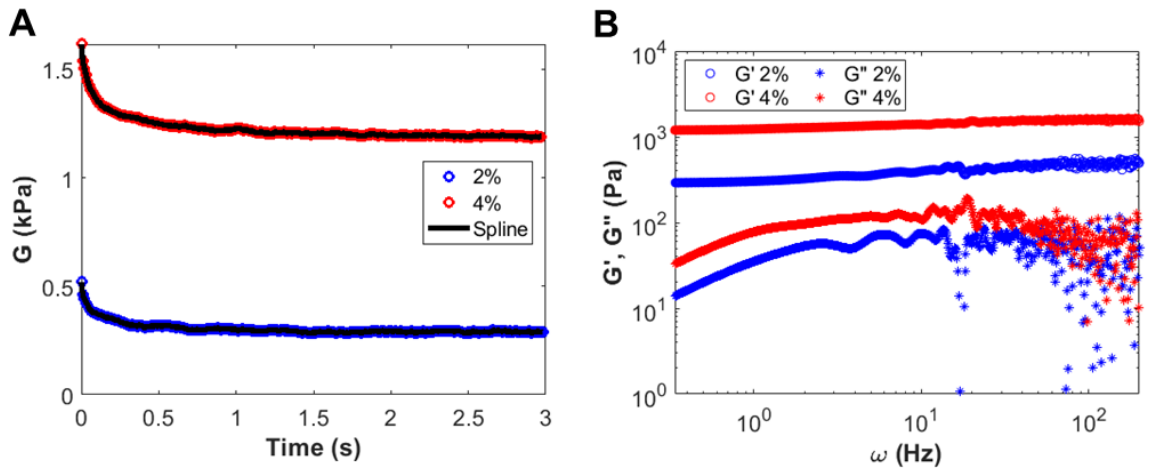

Figure 8. (A) Shear relaxation modulus, $G(t)$, measured over time for EPS DR_{MMW} microgels at 2 and 4% (w/w). Experimental data $G(t)$ was interpolated using the cubic spline method. (B) Storage $G'(w)$ and loss $G''(w)$ moduli obtained by Fourier transforming of $G(t)$.

The mechanical properties of infernan-based microgels measured by AFM showed the elastic moduli between 0.8 kPa and 8 kPa, depending on calcium and EPS concentrations. They are similar to the values reported for other microgels based on synthetic and natural polymers (Oevreeide *et al.*, 2021). $G'(w)$ and $G''(w)$ moduli of these microgels correspond to those usually measured for engineered matrices and soft tissues, such as skin, brain and lung (Chaundhuri, Cooper-White, Janmey, Mooney, & Shenoy, 2020). In general, the elastic modulus of microgels varies between 0.1 and 500 kPa depending on the nature of network crosslinks (e.g. covalent for chemical microgels or non-covalent for physical microgels) and the AFM method used (Oevreeide *et al.*, 2021). In the context of polysaccharide based-microgels crosslinked with Ca^{2+}, alginate represents the most explored natural polymer. Alginate microgels developed for single-cell encapsulation by Mao *et al.* (2016) showed elastic moduli measured by AFM between 0.3 kPa and 16 kPa, depending on alginate molecular weight and calcium concentration used for microgel formulation using microfluidics. In another study, alginate/Ca^{2+} microgels displaying elastic modulus of ~13 kPa (compression tests) were reported (Ahn, Rath, Tsao, Bentley, & Raghavan, 2021). Alginate/Ca^{2+} microparticles obtained

after shrinkage of alginate/Na^+ microdroplets produced using microfluidics showed elastic modulus of ~ 47 kPa (AFM measurements) (Zhang *et al*., 2020). For macroscopic alginate hydrogels crosslinked with calcium and elaborated to study cellular responses in three-dimensional matrices, elastic moduli of ~9 kPa and ~17 kPa (rheological measurements) were reported (Chaundhuri *et al*., 2016). It was shown that a hydrogel with an elastic modulus of 9 kPa induced adipogenesis, while for a higher elastic modulus of 17 kPa, osteogenesis was observed. Alginate/Ca^{2+} hydrogels prepared to assess the effect of mechanical properties (elastic modulus, stress relaxation) on cell spreading and proliferation displayed elastic moduli from 3 kPa to 49 kPa (compressive tests) (Bauer *et al*., 2017). The elastic modulus of hydrogels increased with calcium concentration for the same alginate concentration.

4. Conclusion

In the present study, an experimental approach using a set of AFM-based methods was combined with a theoretical one, exploiting molecular dynamics simulations to investigate the effects of interactions between infernan and Ca^{2+} on the interchain associations and the mechanical properties at two different levels. At the molecular level, AFM imaging was firstly applied to assess the conformational behavior of infernan chains before Ca^{2+} addition. Statistical analysis performed on individual chains allowed to determine their average height of 0.54 ± 0.07 nm and persistence length of 24.8 ± 7.6 nm. The measured structural features of infernan chains agreed well with those obtained from molecular dynamics simulations. Secondly, AFM imaging of infernan chains after Ca^{2+} addition revealed the stacking of several polysaccharide chains. Generated models of chain-chain pairing induced by Ca^{2+}, showing both lateral and twisted chain stacking, perfectly agreed with AFM observations of highly-diluted and less-diluted samples. The ability of infernan chains to associate through Ca^{2+} and form physical gel was further exploited to prepare EPS/Ca^{2+} microgels using microfluidics. In these microgels, further chain-chain association was noticed, as assessed by increasing fiber diameter

observed on SEM images. The impact of chain-chain associations, modulated by different EPS and $CaCl_2$ concentrations, on the mechanical properties of microgels formed was then assessed by AFM. The apparent elastic modulus of microgels measured from force-indentation curves varied from ~1 kPa to ~8 kPa, depending on EPS and $CaCl_2$ concentrations. It appeared that the modulus can be tuned by five-fold, with increasing $CaCl_2$ concentration from 2 mM to 1 000 mM, and by four-fold, with increasing EPS concentration from 2 to 4% (w/w). In addition, the rheological properties of microgels were determined by AFM from the shear relaxation modulus measured over time. The frequency-dependent elastic character of microgels was in good agreement with the elastic modulus values obtained from force-indentation curves. The viscous component was always lower than the elastic one indicating that the microgels did not exhibit a pronounced liquid-like character in the accessible frequency range, between 0.33 Hz and 200 Hz. Finally, by modulating the crosslinking density of the physical network, the resulting mechanical properties of microgels can be tuned to design hydrogels with appropriate properties for specific applications in tissue engineering.

Declarations of interest: The authors declare no conflict of interest.

Acknowledgments

The authors would like to thank Laetitia Marchand for monosaccharide analysis and sulfate content determination.

Financial support was provided by the French National Research Agency within the framework of the *FunCapsul* project (ANR-17-CE08-0001).

Author Contributions:

Agata Zykwinska: Conceptualization, Methodology, Investigation, Formal analysis, Validation, Funding acquisition, Writing – Original Draft, Writing – Review & Editing; **Olga Makshakova**: Conceptualization, Methodology, Investigation, Formal analysis, Writing – Original Draft, Writing – Review & Editing; **Perrine Gélébart**: Investigation, Formal analysis, Writing – Review & Editing; **Corinne Sinquin**: Investigation, Formal analysis, Writing – Review & Editing; **Nicolas Stephant**: Investigation, Formal analysis, Writing – Review & Editing; **Sylvia Colliec-Jouault**: Writing – Review & Editing; **Serge Perez**: Conceptualization, Methodology, Investigation, Formal analysis, Writing – Original Draft, Writing – Review & Editing; **Stéphane Cuenot**: Conceptualization, Methodology; Investigation, Formal analysis, Validation, Writing – Original Draft, Writing – Review & Editing.

References

Ahn, S. H., Rath, M., Tsao, C.-Y., Bentley, W. E., & Raghavan, S. R. (2021). Single-step synthesis of alginate microgels enveloped with a covalent polymeric shell: a simple way to protect encapsulated cells. *Applied Materials & Interfaces*, *13*, 18432-18442.

Augst, A. D., Kong, H. J., & Mooney, D. J. (2006). Alginate hydrogels as biomaterials. *Macromolecular Bioscience, 6*, 623-633.

Bauer, A., Gu, L., Kwee, B., Li, W. A., Dellacherie, M., Celiz, A. D., & Mooney, D. J. (2017). Hydrogel substrate stress-relaxation regulates the spreading and proliferation of mouse myoblasts. *Acta Biomaterialia, 62*, 82-90.

Bergmann, D., Furth, G., & Mayer, C. (2008). Binding of bivalent cations by xanthan in aqueous solution. *International Journal of Biological Macromolecules, 42*, 245-251.

Berry, J. D., Biviano, M., & Dagastine, R. R. (2020). Poroelastic properties of hydrogel microparticles. *Soft Matter*, *16*, 5314.

Bettini, A., Pozzan, M. R., Valdevit, E., & Frontali, C. (1980). Microscopic persistence length of native DNA: its relation to average molecular dimensions. *Biopolymers*, *19*, 1689-1694.

Braccini, I., & Pérez, S. (2001). Molecular basis of $Ca2^{+}$-induced gelation in alginates and pectins: the egg-box model revisited. *Biomacromolecules, 2*, 1089-1096.

Braccini, I., Grasso, R. P., & Perez, S. (1999). Conformational and configurational features of acidic polysaccharides and their interactions with calcium ions: a molecular modeling investigation. *Carbohydrate Research, 317*, 119-130.

Brant, D. A., & Goebel, K. D. (1975). General treatment of configurational statistics of polysaccharides. *Macromolecules, 8*, 522–530.

Caballero Aguilar, L. M., Silva, S. M., & Moulton, S. E. (2019). Growth factor delivery: defining the next generation platforms for tissue engineering. *Journal of Controlled Release*,

306, 40-58. Case, D. A., Darden, T. A., Cheatham, T. E., Simmerling, C. L., Wang, J., Duke, R. E., et al. (2012). AMBER 12. San Francisco: University of California.

Chandhuri, O., Gu, L., Klumpers, D., Darnell, M., Bencherif, S. A., Weaver, J. C., Huebsch, N., Lee, H.-P., Lippens, E., Duda, G. N., & Mooney, D. J. (2016). Hydrogels with tunable stress relaxation regulate stem cell fate and activity. *Nature Materials, 15*, 326-334.

Chaudhuri, O., Cooper-White, J., Janmey, P. A., Mooney, D. J., & Shenoy, V. B. (2020). Effects of extracellular matrix viscoelasticity on cellular behavior. *Nature*, *584*, 535-546.

Cieśla, J., Koczańska, M., Pieczywek, P., Szymańska-Chargot, M., Cybulska, J., & Zdunek, A. (2021). Structural properties of diluted alkali-soluble pectin from *Pyrus communis* L. in water and salt solutions. *Carbohydrate Polymers*, *273*, 118598.

Corolleur, F., Level, A., Matt, M., & Pérez, S. (2020). Innovation potentials triggered by glycoscience research, *Carbohydrate Polymers*, *233*, 115833.

Cros, S., Garnier, C., Axelos, M. A. V., Imberty, A., & Pérez, S. (1996). Solution conformations of pectin polysaccharides: Determination of chain characteristics by small angle neutron scattering, viscometry, and molecular modeling. *Biopolymers*, *39*, 339– 352.

Cuenot, S., Alem, H., Louarn, G., Demoustier-Champagne, S., & Jonas, A. (2008). Mechanical properties of nanotubes of polyelectrolyte multilayers. *The European Physical Journal E, 25*, 343-348.

Cuenot, S., Radji, S., Alem, H., Demoustier-Champagne, S. & Jonas, A. (2012). Control of swelling of responsive nanogels by nanoconfinement. *Small, 8*, 2978.

Cuenot, S., Bouvrée, A., & Bouchara, J.-P. (2017). Nanoscale mapping of multiple lectins on cell surfaces by Single-Molecule Force Spectroscopy. *Advanced Biosystems*, *1*, 1700050.

Darling, E.M., Zauscher, S., Block, J.A., & Guilak, F. (2007). A thin-layer model for viscoelastic, stress-relaxation testing of cells using atomic force microscopy: do cell properties reflect metastatic potential? *Biophys. J.*, *92*, 1784-1791.

673 Decho, A. W. (1999). Imaging an alginate polymer gel matrix using atomic force microscopy.
674 *Carbohydrate Research*, 315, 330-333.
675 Efremov, Y. M., Okajima, T., & Raman, A. (2020). Measuring viscoelasticity of soft biological
676 samples using atomic force microscopy. *Soft Matter*, *16*, 64-81.
677 Evans, R. M. L., Tassieri, M., Auhl, D., & Waigh, T.A. (2009). Direct conversion of rheological
678 compliance measurements into storage and loss moduli. *Physical Review E*, *80*, 012501.
679 Florin, E.-L., Moy, V. T., & Gaub, H. E. (1994). Adhesion forces between individual ligand-
680 receptors pairs. *Science*, *264*, 415-417.
681 Freitas, C. M. P., Coimbra, J. S. R., Souza, V. G. L., & Sousa, R. C. S. (2021). Structure and
682 applications of pectin in food, biomedical and pharmaceutical industry: a review. *Coatings*, *11*,
683 11080922.
684 Gélébart, P., Cuenot, S., Sinquin, C., Halgand, B., Sourice, S., Le Visage, C., Guicheux, J.,
685 Colliec-Jouault, S., & Zykwinska, A. (2022). Microgels based on Infernan, a
686 glycosaminoglycan-mimetic bacterial exopolysaccharide, as BMP-2 delivery systems.
687 *Carbohydrate Polymers*, *284*, 119191.
688 Grant, G. T., Morris, E. R., Rees, D. A., Smith, P. J. C., & Thom, D. (1973). Biological
689 interactions between polysaccharides and divalent cations; the egg-box model. *FEBS Letters*,
690 *32*, 195-198.
691 Haxaire, K., Braccini, I., Milas, M., Rinaudo, M., & Perez, S. (2000). Conformational behavior
692 of hyaluronan in relation to its physical properties as probed by molecular modeling.
693 *Glycobiology*, *10*, 587–594.
694 Hertz, H. (1881). Uber die berührung fester elastischer körper, *Journal für die reine und*
695 *angewandte Mathematik*, *92*, 156-171.
696 Hinterdorfer, P., & Dufrêne, Y. F. (2006). Detection and localization of single molecular
697 recognition events using atomic force microscopy. *Nature Methods*, *3*, 347-355.

Janaswamy, S., & Chandrasekaran, R. (2008). Heterogeneity in iota-carrageenan molecular structure: insights for polymorph II→III transition in the presence of calcium ions. *Carbohydrate Research*, *343*, 364-373.

Jansson, P. E., Kenne, L., & Lindberg, B. (1975). Structure of the extracellular polysaccharide from *Xanthomonas campestris*. *Carbohydrate Research*, *45*, 275-282.

Kirschner, K. N., Yongye, A. B., Tschampel, S. M., Gonzalez-Outeirino, J., Daniels, C. R., Foley, B. L., et al. (2008). GLYCAM06: a generalizable biomolecular force field. Carbohydrates. *Journal of Computational Chemistry*, *29*, 622–655.

Kroon-Batenburg, L. M. J., Kruiskamp, P. H., Vliegenthart, J. F. G., & Kroon, J. (1997). Estimation of the persistence length of polymers by MD simulations on small fragments in solution. Application to cellulose. *The Journal of Physical Chemistry B*, *101*, 8454-8459.

Kumar, A. Rao, K., M., & Han, S. S. (2018). Application of xanthan gum as polysaccharide in tissue engineering: a review. *Carbohydrate Polymers*, *180*, 128-144.

Lambert, F., Milas, M., & Rinaudo, M. (1985). Sodium and calcium counterion activity in the presence of xanthan polysaccharide. *International Journal of Biological Macromolecules*, *7*, 49-52.

Lee, E. H., & Radok, J. R. M. (1960). The contact problem for viscoelastic bodies. *Journal of Applied Mechanics*, *27*, 438-444.

Mahaffy, R. E., Park, S., Gerde, E., Kas, J., & Shih, C. K. (2004). Quantitative analysis of the viscoelastic properties of thin regions of fibroblasts using atomic force microscopy. *Biophysical Journal*, *86*, 1777-1793.

Makshakova, O. N., Zykwinska, A., Cuenot, S., Colliec-Jouault, S., & Perez, S. (2022). Three-dimensional structures, dynamics and calcium-mediated interactions of the exopolysaccharide, Infernan, produced by the deep-sea hydrothermal bacterium *Alteromonas infernus*. *Carbohydrate Polymers*, *276*, 118732.

Mao, A. S., Shin, J.-W., Utech, S., Wang, H., Uzun, O., Li, W., Cooper, M., Hu, Y., Zhang, L., Weitz, D. A., & Mooney, D. J. (2016). Deterministic encapsulation of single cells in thin tunable microgels for niche modelling and therapeutic delivery. *Nature Materials*, *16*, 236-243.

Merceron, C., Portron, S., Vignes-Colombeix, C., Rederstorff, E., Masson, M., Lesoeur, J., Sourice, S., Sinquin, C., Colliec-Jouault, S., Weiss, P., Vinatier, C., & Guicheux, J. (2012). Pharmacological modulation of human mesenchymal stem cell chondrogenesis by a chemically oversulfated polysaccharide of marine origin: Potential application to cartilage regenerative medicine. *Stem Cells*, *30*, 471-480.

Moorhouse, R., Walkinshaw, M. D., & Arnott, S. (1977). Xanthan gum – molecular conformation and interactions. *ACS Symposium Series*, vol. 45, *American Chemical Society*, Washington, DC, 90-102.

Moreno-Guerra, J. A., Romero-Sanchez, I. C., Martinez-Borquez, A., Tassieri, M., Stiakakis, E., & Laurati, M. (2019). Model-free rheo-AFM probes the viscoelasticity of tunable DNA soft colloids. *Small*, *15*, 1904136.

Morris, V. J., Mackie, A., R., Wilde, P. J., Kirby, A. R., Mills, C. N., & Gunning, A. P. (2001). Atomic Force Microscopy as a tool for interpreting the rheology of food biopolymers at the molecular level. *Lebensmittel-Wissenschaft Technologie*, *34*, 3-10.

Nalam, P. C., Gosvami, N. N., Caporizzo, M. A., Composto, R. J., & Carpick, R. J. (2015). Nano-rheology of hydrogels using direct drive force modulation. *Soft Matter*, *11*, 8165-8178.

Noto, R., Martorana, V., Bulone, D., & San Biagio, P. L. (2005). Role of charges and solvent on the conformational properties of poly(galacturonic acid) chains: a molecular dynamics study. *Biomacromolecules*, *6*, 2555-2562.

Oevreeide, I. H., Szydlak, R., Luty, M., Ahmed, H., Prot, V., Skallerud, B. H., Zemla, J., Lekka, M., & Stokke, B. T. (2021). On the determination of mechanical properties of aqueous microgels – towards high-throughput characterization. *Gels*, *7*, 7020064.

748 Pacheco-Quito, E.-M., Ruiz-Caro, R., & Veiga, M.-D. (2020). Carrageenan: drug delivery
749 systems and other biomedical applications. *Marine Drugs*, *18*, 18110583.
750 Raguénès, G., Peres, A., Ruimy, R., Pignet, P., Christen, R., Loaec, M., Rougeaux, H., Barbier,
751 G., & Guezennec, J. G. (1997). *Alteromonas infernus* sp. Nov., a new polysaccharide producing
752 bacterium isolated from a deep-sea hydrothermal vent. *Journal of Applied Microbiology*, *82*,
753 422-430.
754 Rederstorff, E., Rethore, G., Weiss, P., Sourice, S., Beck-Cormier, S., Mathieu, E., Maillasson,
755 M., Jacques, Y., Colliec-Jouault, S., Fellah, B. H., Guicheux, J., & Vinatier, C. (2017).
756 Enriching a cellulose hydrogel with a biologically active marine exopolysaccharide for cell-
757 based cartilage engineering. *Journal of Tissue Engineering and Regenerative Medicine*, *11*,
758 1152-1164.
759 Relini, A., Torrassa, S., Ferrando, R., Rolandi, R., Campioni, S., Chiti, F., & Gliozzi, A. (2010).
760 Detection of populations of amyloid-like protofibrils with different physical properties.
761 *Biophysical Journal*, *98*, 1277-1284.
762 Rivetti, C., Guthold, M., & Bustamante, C. (1996). Scanning force microscopy of DNA
763 deposited onto mica: equilibration versus kinetic trapping studies by statistical polymer chain
764 analysis. *Journal of Molecular Biology*, *264*, 919-932.
765 Roger, O., Kervarec, N., Ratiskol, J., Colliec-Jouault, S. & Chevolot, L. (2004). Structural
766 studies of the main exopolysaccharide produced by the deep-sea bacterium *Alteromonas*
767 *infernus. Carbohydrate Research*, *339*, 2371-2380.
768 Schefer, L., Usov, I., & Mezzenga, R. (2015). Anomalous stiffening and ion-induced coil-helix
769 transition of carrageenans under monovalent salt conditions. *Biomacromolecules*, *16*, 985-991.
770 Subbiah, R., & Guldberg, R. E. (2019). Materials science and design principles of growth factor
771 delivery systems in tissue engineering and regenerative medicine, *Advanced Healtcare*
772 *Materials*, *8*, 1801000.

Vining, K. H., & Mooney, D. J. (2017). Mechanical forces direct stem cell behaviour in development and regeneration. *Nature Reviews*, *18*, 728-742.

Xu, X., Koslowski, M., & Raman, A. (2012). Dynamics of surface-coupled microcantilevers in force modulation atomic force microscopy – magnetic vs dither piezo excitation. *Journal of Applied Physics*, *111*, 054303.

Zdunek, A., Pieczywek, P. M., & Cybulska, J. (2021). The primary, secondary, and structures of higher levels of pectin polysaccharides. *Comprehensive Reviews in Food Science and Food Safety*, *20*, 1101-1117.

Zhang, C., Grossier, R., Lacaria, L., Rico, F., Candoni, N., & Vessler, S. (2020). A microfluidic method generating monodispersed microparticles with controllable sizes and mechanical properties. *Chemical Engineering Science*, *211*, 115372.

Zykwinska, A., Marquis, M., Godin, M., Marchand, L., Sinquin, C., Garnier, C., Jonchère, C., Chédeville, C., Le Visage, C., Guicheux, J., Colliec-Jouault, S., & Cuenot, S. (2019). Microcarriers based on glycosaminoglycan-like marine exopolysaccharide for TGF-β1 long-term protection. *Marine Drugs*, *17*, 1–15.

Zykwinska, A., Marquis, M., Sinquin, C., Marchand, L., Colliec-Jouault, S., & Cuenot, S. (2018). Investigation of interactions between the marine GY785 exopolysaccharide and transforming growth factor-β1 by atomic force microscopy. *Carbohydrate Polymers*, *202*, 56–63.

Zykwinska, A., Gaillard, C., Boiffard, M.-H., Thibault, J.-F., & Bonnin, E. (2009). "Green labelled" pectins with gelling and emulsifying properties can be extracted by enzymatic way from unexploited sources. *Food Hydrocolloids*, *23*, 2468-2477.